Experimental and modeling study of the pyrolysis and combustion of dimethoxymethane

Florence H Vermeire, Hans-Heinrich Carstensen, Olivier Herbinet, Frédérique Battin-Leclerc, Guy B Marin, Kevin M van Geem

Experimental and modeling study of the pyrolysis and combustion of dimethoxymethane

Florence H. Vermeire[1], Hans-Heinrich Carstensen[1], Olivier Herbinet[2], Frédérique Battin-Leclerc[2], Guy B. Marin[1], Kevin M. Van Geem[1],*

[1] *Laboratory for Chemical Technology, Ghent University, Technologiepark 914, 9052 Gent, Belgium*
[2] *Laboratoire Réactions et Génie des Procédés, CNRS, Universite de Lorraine, Nancy, France*

Published in Combustion and Flame, Volume 190, April 2018, Pages 270–283

Abstract

The pyrolysis and low- to intermediate temperature oxidation chemistry of dimethoxymethane (DMM), the simplest oxymethylene ether, is studied theoretically and experimentally in a JSR setup. The potential energy surfaces for peroxy species relevant during the low-temperature oxidation of dimethoxymethane are studied at the CBS-QB3 level of theory and the results are used to calculate thermodynamic properties of the main species as well as rate expressions for important reactions. An elementary step model for DMM pyrolysis and oxidation is built with the automatic kinetic model generation software Genesys. To describe the chemistry of small species not directly related to DMM, the AramcoMech 1.3 mechanism developed by Metcalfe et al. is used. If the more recently extended version of this mechanism, i.e. the propene oxidation mechanism published by Burke et al., was used as alternative base mechanism, large discrepancies for the mole fractions of CO_2, methyl formate and methanol during the pyrolysis of DMM were observed. The validation of the new DMM model is carried out with new experimental data that is acquired in an isothermal quartz jet-stirred reactor at low and intermediate temperatures. Different equivalence ratios, φ = 0.25, φ = 1.0, φ = 2.0 and φ = ∞, are studied in a temperature range from 500 K to 1100 K, at a pressure of 1.07 bar and with an inlet DMM mole fraction of 0.01. The experimental trends are well predicted by the model without any tuning of the model parameters although some improvements are possible to increase quantitative agreement. The largest discrepancies are observed at fuel lean conditions for the hydrocarbon mole fractions, and at low-temperatures as can be noticed by the over prediction of formaldehyde and methyl formate. The kinetic model is also validated against plug flow reactor, jet-stirred reactor and lean and rich premixed flames data from the literature. Rate of production analyses are performed to identify important pathways for low- and intermediate-temperature oxidation and pyrolysis.

Keywords: Dimethoxymethane; Oxymethylene ethers; Potential energy surface; Low-temperature oxidation; Jet-stirred reactor

1. Introduction

Environmental issues like the urge to reduce the emission of greenhouse gases and particulate matter create concerns that encourage the research on alternative fuels or the use of additives. Diesel engines are known for their high fuel efficiency, but also for their higher emission of toxic exhaust gases like polycyclic aromatic hydrocarbons and NOx. By blending diesel fuels with oxygenated additives emission levels can be reduced [1-4]. For example, blends of diesel with ethanol and biodiesel are worldwide used and their beneficial effect on emissions has frequently been demonstrated [5]. It is found that compared to conventional diesel, emissions of carbon monoxide, unburned hydrocarbons and particulate matter are reduced, while NOx emissions tend to increase [6].

Dimethyl ether (DME) is another potential clean fuel additive. The addition of DME to diesel reduces smoke emissions depending on the operating conditions and NOx, carbon monoxide and unburned hydrocarbon emissions are lower for most operating conditions [7]. However, the increased vapor pressure, the lower viscosity and a limited solubility at lower temperatures prevent the use of diesel/DME mixtures in conventional diesel engines [7]. The oxidation chemistry of DME has been studied extensively as summarized by Rodriguez et al. [8]

The emission reduction of oxygenates is thought to be related to the C-O bonds found in these molecules. A polyether such as poly(oxymethylene) dimethyl ethers (also oxymethylene ethers, OMEs or CH_3-O-$(CH_2$-O$)_n$-CH_3 should be an even more efficient additive and the few available studies support this conclusion [9-15]. These oxygenates open a new route for enhancing diesel properties. Especially OMEs with a chain length of n = 3,4 are attractive fuel additives, as they can be produced from the sole feedstock methane with gas-to-liquid technology. Their miscibility with diesel fuels allows these blends directly to be used in existing diesel engines without the need for technical modifications [12].

Studies on the oxidation chemistry of OMEs are scarce. Some attention has been paid to the oxidation of the simplest OME, dimethoxymethane (also methylal or DMM) with chain length n = 1. Daly et al. [16] performed experiments in a jet-stirred reactor to study the oxidation of DMM at intermediate temperatures ranging from 800 to 1200 K, 5.07 bar and at various equivalence ratios. Daly et al. also developed a kinetic model, which relies mainly on kinetic parameters that are estimated by analogies to reactions of hydrocarbons, dimethyl ether and diethyl ether. Despite these approximations, their model predicts the observed product mole fractions reasonably well. Lean and rich DMM flames have been studied by Dias et al. [17-19] and a kinetic model was developed in order to simulate the DMM flame data. The kinetic parameters were taken from literature, mainly from the work of Daly et al. [16] Recently, experiments in a plug flow reactor at atmospheric and high pressures were reported by Marrodán et al. [20,21] Their experiments were performed for a large temperature range, 373 –1073 K, and air excess ratios ranging from 0.7 to 20. A kinetic model was developed by combining in-house kinetic models for small hydrocarbons such as DME, ethanol, acetylene and methyl formate with the slightly modified kinetic model developed by Dias et al. for DMM [17-19]. The agreement between experimental data and model predictions is reasonable but not perfect, suggesting that the DMM chemistry is not yet fully understood.

In this work the pyrolysis and oxidation chemistry of DMM is studied in detail experimentally and through simulations using a newly developed kinetic model. This model distinguishes itself from prior models through the use of ab initio calculated thermodynamic properties for important species and rate expressions for crucial reactions. In this context, the potential energy surfaces relevant for the low-temperature oxidation are investigated

in detail. A large part of the comprehensive kinetic model is constructed automatically with Genesys [22,23]. Experiments are performed in an isothermal quartz jet-stirred reactor for temperatures ranging from 500 to 1100 K, at a pressure of 1.07 bar, studying pyrolysis as well as three oxidizing conditions to validate the new kinetic model. Rate of production analyses are presented at 650 and 700 K to explain the low-temperature reactivity in oxidizing environments. Furthermore, rate of production analyses performed at 900 K for both oxidizing and pyrolysis conditions are used to identify chemistry differences between oxidation and pyrolysis conditions. Finally, sensitivity analyses are employed to identify reactions that may be responsible for discrepancies between observed and predicted mole fractions.

2. Experimental methods

The pyrolysis and oxidation of dimethoxymethane are studied in an isothermal quartz jet-stirred reactor. The main features of the experimental apparatus are summarized below. Details regarding the set-up can be found elsewhere [24].

Helium (Messer, 99.99%) and dimethoxymethane (Sigma-Aldrich, 99%) are passed through an evaporator and mixed. Downstream, oxygen (Messer, 99.999%) is added to the gaseous flow. The helium and oxygen flow rates are controlled by gas-mass-flow controllers (Bronkhorst IN-FLOW) and the liquid fuel mass flow rate is regulated by liquid-Coriolis-flow controllers (Bronkhorst M12).

The gaseous mixture passes through an annular preheating zone, where it is heated to the reactor temperature, and enters the jet-stirred reactor through four nozzles. The nozzles and reactor are designed to limit as much as possible thermal and concentration gradients. Thermocoax resistance wires provide heating for the annular preheating zone and the reactor. A type K thermocouple measures the temperature in the center of the reactor (measured temperature gradients < ± 5 K). The pressure is set with a needle valve downstream of the reactor.

The reactor outlet is connected to three gas chromatographs (GC) that allow online quantification of product species. The transfer lines to the GCs are kept at 433 K to avoid condensation. The first GC is used to detect O_2, CO, CO_2 and CH_4 in case of oxidation and H_2 in case of pyrolysis. This GC is equipped with a Carbosphere packed column and a thermal conductivity detector. If H_2 needs to be detected at pyrolysis conditions, Ar is used as carrier gas, otherwise the carrier gas is He. The second GC contains a PLOT-Q capillary column and a flame ionization detector (FID) preceded by a methanizer. The methanizer enables the detection of species like CO, CO_2 and formaldehyde with the FID. The third GC has a HP-5 ms capillary column installed and is equipped with a FID. A GC connected to a mass spectrometer (GC–MS) is used for either online or offline product identification. The GC–MS is operated either with a PLOT-Q or with a HP-5 ms capillary column. The MS is a quadrupole mass spectrometer with a mass range of 10–400 m/z. Products are quantified by either injecting known amounts of pure samples into the GCs or by applying the effective carbon number method. The relative experimental error of the compound mole fraction determined by injecting a known amount of the pure substance is 5% based on experience. When the effective carbon number method is applied, the relative experimental error is estimated to be 10%.

The volume of the quartz reactor is 85 cm^3. During experiments, the volumetric flow rate in the reactor, calculated with the total molar inlet flow rate and the temperature and pressure in the reactor, is set to 3.0×10^{-5} m^3 s^{-1}, which corresponds to a residence time of 2.83 s. The temperature ranges from 500 to 1100 K and the pressure is kept at

1.07 bar. The DMM inlet mole fraction equals 0.01 for all experiments. Four equivalence ratios, φ = 0.25, φ = 1.0, φ = 2.0 and φ = ∞, are investigated. 21 species are identified and quantified with the online gas chromatographs. The carbon balances are closed within 5% at most conditions. Since the analysis section does not allow quantifying water and hydrogen peroxide, the hydrogen and oxygen elemental balances are not available. A spreadsheet of the experimental results is provided in the Supporting information.

3. Computational method

Electronic structure calculations are performed on the high-performance supercomputer at Ghent University at the CBS-QB3 level of theory [25] as implemented in Gaussian 09 [26]. The lowest energy conformers are determined manually by carrying out calculations for the most likely structures at the B3LYP/6-31G(d) level of theory, for most species and transition states. For more complex molecules and transition states, in which several hydrogen bonds are present, in-house developed algorithms are used to automatically search for the lowest energy conformer [27].

The CBS-QB3 results are used to calculate the heat capacities at different temperatures, the standard entropy and the standard enthalpy of formation. Internal modes are treated as harmonic oscillators except for modes that resemble rotations around single bonds. The latter are approximated by 1-dimensional hindered internal rotations (1D-HIR). All single bonds and bonds in the reactive moiety of the transition state are treated this way as long as the hindrance potential does not exceed 40 kJ mol−1. The hindrance potentials are calculated at the B3LYP/6-31G(d) level of theory with relaxed surface scans in which all coordinates, except for the dihedral angle of interest, are re-optimized at each scan angle. The Fourier series expression of the hindrance potential together with reduced moment of inertia calculated at the $I^{(2,3)}$ level, as defined by East and Radom [28], are used to construct the Schrödinger equation for 1-dimensional internal rotation. The eigenvalues of the solution are used to determine the partition function as a function of temperature. The thermodynamic data is calculated from the total partition function after correction for the symmetry and the number of optical isomers. For the calculation of the enthalpy of formation, the atomization method is applied. The systematic errors of the enthalpy of formation calculated at the CBS-QB3 level of theory are corrected by applying spin-orbit corrections (SOC) [29] as these are not part of the CBS-QB3 methodology, and empirically by applying bond additive corrections (BAC) [30]. But note that the enthalpy values used for PES construction and to calculate rate coefficients are not BAC corrected because only relative enthalpies are needed. Moreover, BAC corrections are not defined for transition state bonds. The conventional transition state theory is applied to calculate the rate coefficients over a temperature range 300 – 1500 K with 50 K increment. Tunneling is accounted for using the asymmetric Eckart potential [31]. The resulting rate coefficients are regressed to a modified Arrhenius expression.

The uncertainty on theoretical calculations for one specific species or reactions can be calculated as reported by Prager et al. [32]. To determine the estimated uncertainty with this method, theoretical calculations are required at different levels of theory which are computationally intensive. As this is not the focus of this work, such detailed assessment is not done. A general assessment of the uncertainty on theoretical calculations with the method used in this work can be made based on previous studies using the same methodology. Paraskevas et al. [33] evaluated the uncertainty on thermodynamic data determined at the CBS-QB3 level of theory for oxygenates by the comparison with experimental data. From this study it can be concluded that the calculated enthalpies of formation at 298 K are, generally, determined within 4 kJ mol^{-1} and entropies are expected to be well reproduced. Villano et al. [34] used the same methodology applied in this study to investigate the bond strengths of alkylperoxy radicals and showed

that the results are within a few kJ mol−1 of experimental data. A similar accuracy is expected in this work. The calculated BAC and SOC corrected enthalpies of formation for DMM (−346 kJ mol^{-1}) and DME (−183 kJ mol^{-1}) are indeed close to the corresponding entries in the NIST Chemistry Webbook (−348.2 ± 0.79 kJ mol^{-1} and 184.1 ± 0.5 kJ mol^{-1}, respectively). Carstensen and Dean studied the hydrogen abstraction reaction from methane by a hydrogen atom [35] and the CO elimination from phenoxy radicals [36] at the CBS-QB3 level of theory. For both case studies, the deviation between the theoretical and experimental rate coefficients is within a factor 2. Vandeputte et al. [37] assessed the reliability of two composite methods and two density functional theory methods for the determination of kinetic parameters. Also the influence the internal hindered rotor treatment and the effect of tunneling is studied. The best agreement with experimental data is obtained with the CBS-QB3 level of theory combined with 1D-HIR corrections and Eckart tunneling. With this approach, the uncertainty on the kinetic data between 600 and 1000 K is below a factor of 4. Based on these studies, the uncertainty on the kinetic data determined at the CBS-QB3 level of theory is assumed to be within a factor 2-4. Note that the larger factor of 4 accounts for uncertainties in entropy values caused by the coupling of internal rotors due to hydrogen bonds.

A complete list of the thermodynamic properties and the modified Arrhenius parameters calculated in this work at the CBS-QB3 level of theory is provided in the Supporting information.

4. Kinetic model development

A new elementary step model is developed for the pyrolysis and oxidation of dimethoxymethane. The generation is done in three steps. First, electronic structure calculations are performed for species and reactions related to paths that are believed to be important for the DMM chemistry. The results are discussed in paragraph 5.1. The thermodynamic properties and kinetic parameters derived from these calculations are added to databases, which collect ab initio calculation results performed in our research group.

Second, the automatic kinetic model generation tool Genesys [22,23] is used to generate a complete kinetic model for DMM pyrolysis and oxidation. Starting from a number of input species and user-defined reaction families, Genesys automatically generates a kinetic network consisting solely of elementary step reactions. These reactions are implemented as reversible reactions to account for the thermodynamic consistency of the kinetic model. A rule-based termination criterion is used to limit the size of the network. The rules or constraints are applied to the reaction families and the product species. Once the network is completed, thermodynamic and kinetic parameters are assigned to all species and reactions, respectively. Entries from the ab initio databases are used whenever available. If entries for thermodynamic parameters are missing, Benson's group additivity method [38] and Lay's hydrogen bond increment method [39] are applied. The group additive values and hydrogen bond increments used in this work are those calculated by Sabbe et al. [40,41] for hydrocarbons and by Paraskevas et al. [33] for oxygenates. In the case that kinetic entries are not available in the ab initio databases, the group additivity method developed by Saeys et al. [42] and extended by Sabbe et al. [41] or analogies to similar reactions are used to calculate the Arrhenius parameters. For hydrogen abstraction reactions, the group additive values determined by Sabbe et al. [43] for hydrocarbons and by Paraskevas et al. [44,45] for oxygenates are used. For β-scission reactions that involve only carbon and hydrogen atoms in the reactive moiety, group additive values are obtained from Sabbe et al. [41,46] and Paraskevas et al. [47]. The Arrhenius parameters for α-scission with the formation of CO and β-scission reactions that involve oxygen atoms in the reactive moiety are determined by analogies with similar reactions. Since no group additivity data are available for hydrogen abstraction reactions by hydroxyl and hydroperoxy radicals and oxygen

atoms. Here, analogies with alkanes are used [48,49]. For low-temperature oxidation, the reaction families as proposed by Sarathy et al. [50] are selected. Arrhenius parameters for the low-temperature reactions are estimated by reactivity-structure-based rate rules, determined by Cai et al. [49] or Bugler et al. [51] for alkanes, in case no entries are available in the databases.

Third, the automatically generated kinetic model and the AramcoMech 1.3 mechanism, developed by Metcalfe et al. [52], are merged. The AramcoMech 1.3 contains 124 species and 766 reactions and serves as base mechanism to describe the combustion chemistry of small hydrocarbons and oxygenates. In the case that the same species or reaction appears in both the Genesys and the base mechanism, generally the entries of AramcoMech 1.3 are retained. However, the opposite is true for all DMM, dimethyl ether (DME) and methyl formate related species and reactions. The complete kinetic model has 351 species and 2904 reactions and is available in the Supporting information in CHEMKIN [53] format.

It should be noted that the AramcoMech 1.3 mechanism was chosen over a more recently extended version, i.e. the propene oxidation mechanism by Burke et al. [54]. The latter mechanism was also considered to describe the chemistry of the small species during the pyrolysis of DMM but the predictions were poorer compared to the ones with AramcoMech 1.3. A comparison of the model performance for both base mechanisms is given in the Supporting information. Using the propene oxidation mechanism by Burke et al. [54] as base mechanism, the model clearly over-predicts CO_2 and methyl formate mole fractions while methanol is not produced according to the model. The underperformance of Burke's propene oxidation model as base mechanism is explained by the reaction $CH_3OCHO(+ M) = CO + HOCH_3(+ M)$, which is included in the AramcoMech 1.3 mechanism but is missing in Burke's propene oxidation mechanism. Furthermore, the rate coefficients for the important reactions $CH_3OCO = CO + OCH_3$ and $CH_3OCO = CO_2 + CH_3$ differ. After comparison with literature data [55] and in-house calculated rate coefficients the AramcoMech 1.3 mechanism is selected as base mechanism for the final kinetic model.

5. Results and discussion

5.1. Potential energy surface for low-temperature oxidation

The initial step during the DMM oxidation is a hydrogen abstraction reaction by molecular oxygen. The consecutive chemistry of the formed radicals, e.g. their unimolecular decompositions and their reactions with molecular oxygen become very important. In this section, the potential energy surfaces for the addition of molecular oxygen to methoxymethoxymethyl (COCOC•) and dimethoxymethyl (COC•OC), i.e. the primary and secondary radicals formed from dimethoxymethane, respectively, are discussed. The relevant parts of the potential energy surfaces are given in Figures 1 and 2. The potential energy surface for the radicals formed from DMM is provided in the Supporting information. The CBS-QB3 calculated enthalpies of formation at 298 K of COCOC• (−170.0 kJ mol^{-1}) and COC•OC (−169.9 kJ mol^{-1}) are found to be approximately the same even though one is a primary and the other a secondary radical. Based on analogy with alkyl radicals, one would have expected the secondary radical to be more stable than the primary radical.

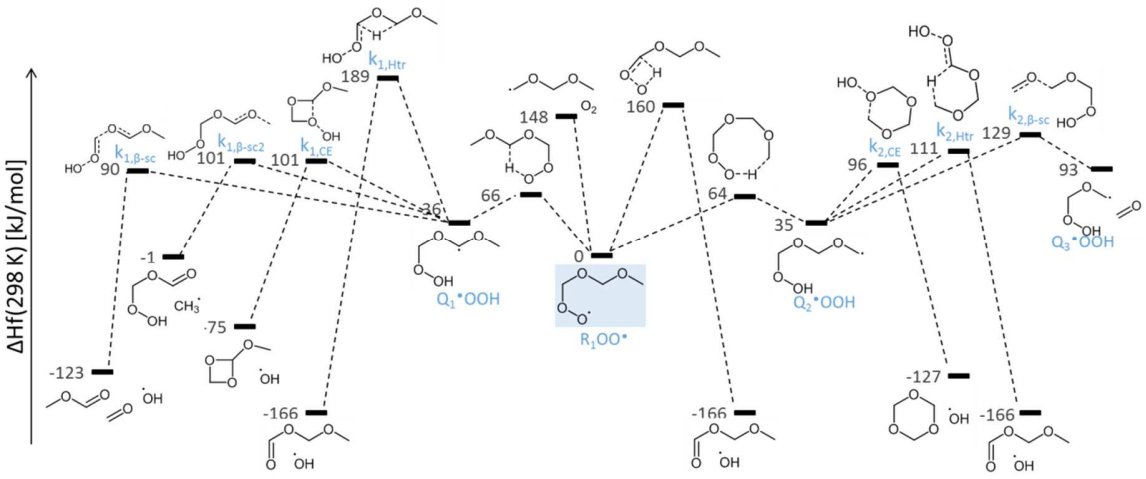

Figure 1: Relevant part of the potential energy surface for the addition of molecular oxygen to the methoxymethoxymethyl radical, i.e. the primary radical formed after hydrogen abstraction from dimethoxymethane. The values are enthalpies of formation calculated at the CBS-QB3 level of theory at 298 K relative to $R_1OO•$.

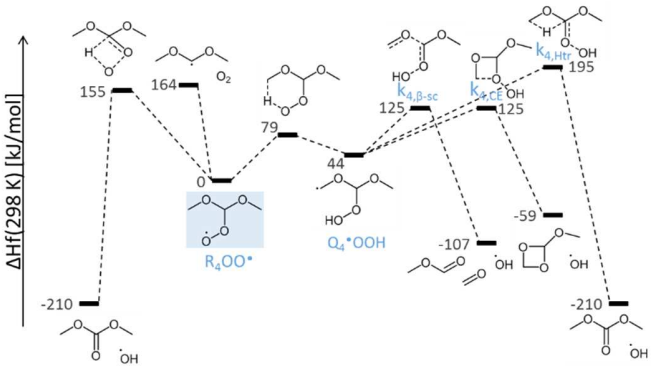

Figure 2: Relevant part of the potential energy surface for the addition of molecular oxygen to the dimethoxymethyl radical, i.e. the secondary radical formed after hydrogen abstraction from dimethoxymethane. The values are enthalpies of formation calculated at the CBS-QB3 level of theory at 298 K relative to $R_4OO•$.

The addition of molecular oxygen to the methoxymethoxymethyl radical produces the peroxide COCOCOO•, labeled $R_1OO•$. The enthalpy of reaction equals 148 kJ mol^{-1}, meaning that the C-OO• bond strength is comparable to those in ethyl peroxy and *n*-propyl peroxy radicals. $R_1OO•$ can react through three different pathways. First, isomerization and subsequent β-scission can occur through a four-membered cyclic transition state, yielding methoxymethyl formate and a hydroxyl radical. The transition state for this reaction is tight and has a higher energy compared to the addition of molecular oxygen to the methoxymethoxymethyl radical. For this reason, this reaction can safely be ignored.

In a second pathway, a hydrogen atom migrates from the secondary carbon atom to the peroxy group forming COC•OCOOH (Q_1•OOH). The six-membered cyclic transition state structure is only 66 kJ mol^{-1} higher than $R_1OO•$. Q_1•OOH can further react by four pathways, i.e. (i) hydrogen migration and subsequent β-scission of the unstable intermediate yield methoxymethyl formate and a hydroxyl radical, (ii) cyclic ether formation yields methoxy-1,3-dioxetane and a hydroxyl radical, (iii) β-scission in the methoxy group leads to a methyl radical and hydroperoxy

methyl formate and (iv) by a β-scission in the hydroperoxymethoxy group, methyl formate, formaldehyde and a hydroxyl radical are formed. It should be noted that the first channel has a significantly higher barrier compared to the other channels and is not important, while the barriers of the other three channels are easily accessible and comparable to competing product channels on this PES. Note that the O-OH bond in hydroperoxy methyl formate is rather weak (the bond dissociation enthalpy at 298 K of 190 kJ mol^{-1} is comparable to the one of alkyl hydroperoxides) and hence the bond breaks easily forming a hydroxyl radical and a second radical. Consequently, Q_1•OOH decomposition via β-scission with the formation of hydroperoxy methyl formate and a methyl radical causes chain branching without the addition of a second molecular oxygen.

The third reaction channel for R_1OO• is a hydrogen atom migration from the primary carbon atom to the peroxide group, forming C•OCOCOOH (Q_2•OOH). This transition state has an eight membered cyclic structure, which is 64 kJ mol^{-1} above R_1OO•. Q_2•OOH reacts through three different pathways. These pathways are cyclic ether formation, isomerization though a six-membered cyclic transition state to an unstable α-hydroperoxyl radical that immediately breaks apart, and β-scission. These reactions form trioxane and a hydroxyl radical, methoxymethyl formate and a hydroxyl radical and formaldehyde and Q_3•OOH, respectively, as can be seen in Figure 1. Since all transition states are of comparable energy and a clear discrimination based on entropic properties is also not possible, it is expected that all pathways might contribute to the Q_2•OOH consumption.

Molecular oxygen adds to the dimethoxymethyl radical to form the peroxide COC(OO•)OC, labeled R_4OO• in Figure 2. The bond enthalpy at 298 K of the formed peroxy bond is surprisingly high (164 kJ mol^{-1}) and clearly exceeds that of the C-OO• bond in R_1OO•, despite the high density of oxygen atoms around the secondary carbon atom in R_4OO•. R_4OO• can react via two pathways. In the first pathway, an isomerization is followed by a β-scission of the unstable intermediate to dimethyl carbonate and a hydroxyl radical. The energy of the four-membered cyclic transition state structure is 155 kJ mol^{-1} higher than the one of R_4OO•. Because the barrier is close to the energy of the peroxy bond and the transition state is very tight, it is safe to ignore this channel. The second channel is hydrogen atom migration to COC(OOH)OC• (Q_4•OOH). The energy for the six-membered cyclic transition state structure for this reaction is only 79 kJ mol^{-1} higher than for R_4OO•. Q_4•OOH further reacts via one of three possible channels. The first pathway produces methyl formate, formaldehyde and a hydroxyl radical via a β-scission reaction. The second channel produces the cyclic ether methoxy-1,3-dioxetane together with a hydroxyl radical. The third channel yields dimethyl carbonate and a hydroxyl radical via intramolecular hydrogen atom shift followed by a β-scission reaction. The high barrier for the last reaction is clearly above the entrance channel and can be safely disregarded.

It is interesting to compare some reactions shown in Figures 1 and 2 with those for alkylperoxy radicals. COCOC• addition to O_2 is exothermic by approximately 148 kJ mol^{-1}. The same bond dissociation enthalpy at 298 K is observed for the analogue CCCCC• addition to O_2 or general primary alkyl radicals [34], even though the corresponding C-H bond in COCOC (410 kJ mol^{-1}) is about 10–15 kJ mol^{-1} weaker than a typical primary C-H bond in alkanes. As mentioned before, the secondary fuel radical (COC•OC) has a similar stability as the primary fuel radical COCOC•. This bond dissociation enthalpy of 410 kJ mol^{-1} is close to that of secondary alkyl radicals, e.g. the BDE for the central secondary carbon atom in CCCCC is around 414 kJ mol^{-1}. The corresponding bond enthalpies at 298 K for the peroxy radicals are 164 kJ mol^{-1} for COC(OO•)OC and 157 kJ mol^{-1} for CCC(OO•)CC. This shows that (a) as seen in alkyl peroxy radicals, the secondary site leads to stronger ROO• bonds and that (b) the secondary peroxy radical of DMM is clearly more stable than the corresponding alkyl peroxy radical with respect to re-dissociation. The NTC region of DMM should thus be shifted towards higher temperatures.

Another interesting feature is the lack of hydroperoxy radicals forming pathways, which play an important role in alkane oxidation chemistry. This is of course easily understood by the fact that no C-H groups are available in β-position to the peroxy group. Instead, next to cyclic ether formation, several additional low-barrier channels that form hydroxyl radicals exist that have rather high barriers in analogous alkyl peroxy chemistry (see e.g. [56]). Hydroxyl radicals can play a more pronounced role in DMM oxidation while hydroperoxyl radical chemistry might be less relevant. Additionally, hydroxyl radicals are formed as a product in the decomposition of unstable R•OOH intermediates, which also produce aldehydes or esters. Moreover, it is important to note that except for 1,3-hydrogen atom shift reactions, all isomerization reactions proceed through barriers that are low compared to the O_2 addition channel, and hence will compete only at higher temperatures with the re-dissociation reaction.

The barrier heights (E0K + ZPE) for isomerization reactions and reactions with the formation of a cyclic ether are compared to the ones determined by Villano et al. [57]. The barrier height (E0K + ZPE) for the 1,5-hydrogen atom shift reaction of COCOCOO• (R_1OO•) is equal to 35 kJ mol^{-1} and very similar to the one from CCCCOO•, equal to 34 kJ mol^{-1}. On the other hand, a large difference is observed between the barrier heights for the 1,5-hydrogen atom shift reaction with abstraction from the primary radical. For COC(OO•)OC (R_4OO•) the barrier height is equal to 42 kJ mol^{-1} and for CCC(OO•)C, equal to 31 kJ mol^{-1}. This is in line with difference in the C-H bond dissociation enthalpies between DMM and typical hydrocarbons as discussed above. The barrier height for the formation of a cyclic ether and a hydroxyl radical from COC•OCOOH (Q_1•OOH) is 66 kJ mol^{-1}, while for CC•CCOOH the barrier is 72 kJ mol^{-1}. A higher barrier is observed for COC(OOH)OC• (Q_4•OOH), equal to 84 kJ mol^{-1}, which is similar to that for the corresponding cyclization of C•CC(OOH)C (81 kJ mol^{-1}).

From the comparison between bond dissociation enthalpies for C-H, C-OO and O-OH bonds and barrier heights for reactions relevant during the low temperature oxidation for alkanes and oxygenates, it can be concluded that although sometimes similar BDE and barrier heights are observed, the relative importance can be very different and hence, rate rules developed for alkanes should not be used for oxygenates.

Instead of decomposing, Q_1•OOH, Q_2•OOH and Q_4•OOH may add to a second molecular oxygen to form HOOCOC(OO•)OC (•OOQ_1OOH), HOOCOCOCOO• (•OOQ_2OOH) and COC(OOH)OCOO• (•OOQ_4OOH) radicals, respectively. The potential energy surfaces for the relevant pathways of these radicals are presented in Figures 3 and 4.

•OOQ_1OOH is formed after addition of molecular oxygen to Q_1•OOH. The bond dissociation enthalpy at 298 K of the newly formed bond is 168 kJ mol^{-1}, which is very similar to that found in R_4OO•. •OOQ_1OOH can react via four different channels that are presented in Figure 3. A hydrogen atom shift from the primary carbon atom to the peroxy group results in the radical HOOCOC(OOH)OC• ($HOOU_1$•OOH). The transition state for this reactions has a six-membered cyclic structure and an enthalpy of 78 kJ mol−1 higher than that of •OOQ_1OOH. $HOOU_1$•OOH can further react via a β-scission reaction with the formation of hydroperoxy methyl formate, formaldehyde and a hydroxyl radical. Two other channels result in the formation of cyclic ethers and a hydroxyl radical. The first cyclic ether is a hydroperoxymethoxy substituted 1,3-dioxetane. It is formed through a four-membered transition state with an energy comparable to that for the hydroperoxy methyl formate forming channel. The second cyclic ether is hydroperoxytrioxane, which is formed through a six-membered cyclic transition state. The barrier for this reaction is only 10 kJ mol^{-1} lower than that for the substituted 1,3-dioxetane channel. All barriers of the discussed subsequent

reactions of $HOOU_1$•OOH are clearly higher than the reverse isomerization barrier to •OOQ_1OOH suggesting that the product channels via $HOOU_1$•OOH are likely unimportant.

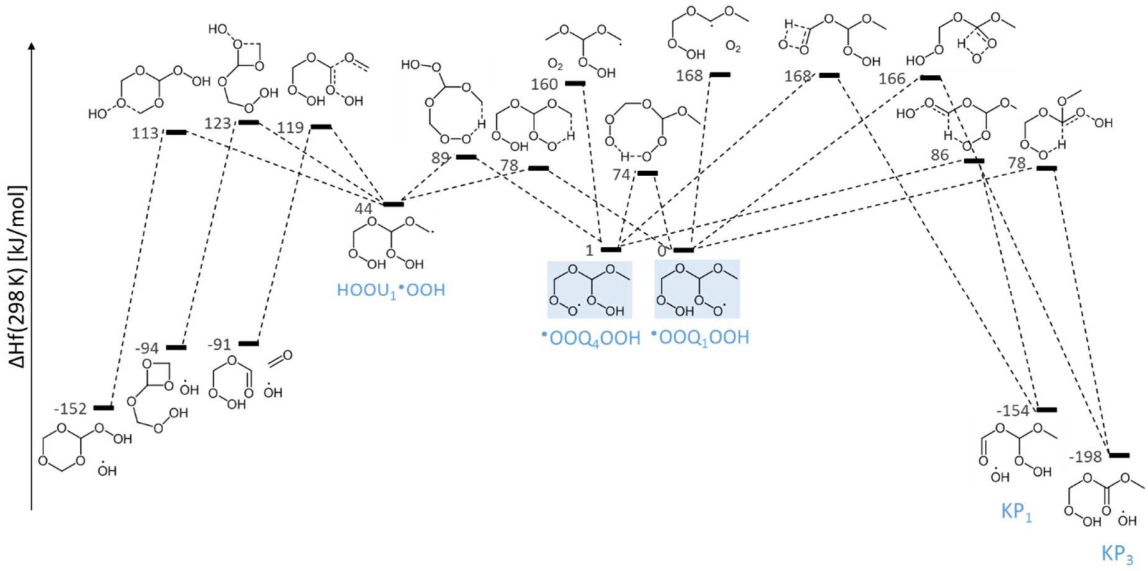

Figure 3: Relevant part of the potential energy surface for •OOQ_1OOH and •OOQ_4OOH, which are formed after the addition of molecular oxygen to Q_1•OOH and Q_4•OOH. The values are enthalpies of formation calculated at the CBS-QB3 level of theory at 298 K relative to •OOQ_1OOH.

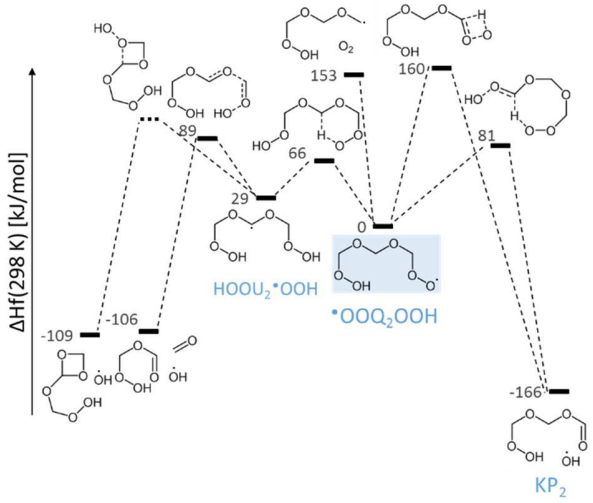

Figure 4: Relevant part of the potential energy surface for •OOQ_2OOH, which are formed after the addition of molecular oxygen to Q_2•OOH. The values are enthalpies of formation calculated at the CBS-QB3 level of theory at 298 K relative to •OOQ_2OOH.

The second •OOQ_1OOH consuming reaction is an intramolecular hydrogen abstraction by the peroxy group from the carbon atom that is bond to the hydroperoxy group. This reaction produces the unstable radical HOOC•OC(OOH)OC which directly dissociates to the keto-hydroperoxide (KP_3) and a hydroxyl radical. The barrier of this reaction is rather high and equal to 166 kJ mol^{-1} and the transition state is tight. The third channel is an isomerization reaction from •OOQ_1OOH to •OOQ_4OOH, hence a hydrogen atom transfer from the hydroperoxy group to the peroxy group.

The low barrier for this reaction is 74 kJ mol^{-1} and implies that both isomers rapidly interconvert. Note that both isomers have approximately the same energy and are also structurally similar. Therefore their concentrations should be comparable. The last channel results in the formation of the keto-hydroperoxide KP_1 and a hydroxyl radical by a hydrogen shift and β-scission of the unstable intermediate. This reaction has a barrier of 86 kJ mol^{-1}. Based on the energies and transition state structures, one would expect that the last two channels dominate the •OOQ_1OOH consumption.

The addition of molecular oxygen to Q_4•OOH yields •OOQ_4OOH. The enthalpy of the formed bond is 160 kJ mol^{-1}, which is clearly higher compared to the bond enthalpy at 298 K found for the first addition of molecular oxygen to methoxymethoxymethyl (148 kJ mol^{-1}). •OOQ_4OOH reacts via four channels, i.e. (i) isomerization to $HOOU_1$•OOH via a low barrier, (ii) the formation of a keto-hydroperoxide (KP_1) and a hydroxyl radical via a tight four-membered cyclic transition state with a high energy, (iii) isomerization to •OOQ_1OOH and (iv) intramolecular hydrogen abstraction followed by a β-scission to form a keto-hydroperoxide (KP_3) and a hydroxyl radical. Except for the second pathway, all other pathways will likely contribute to the consumption of •OOQ_4OOH and thus need to be evaluated. The main conclusions from this PES are that only the product channels leading KP_1 or KP_3 and a hydroxyl radical appear to be competitive and that both second O_2 addition products will rapidly interconvert.

Finally, the addition of molecular oxygen to Q_2•OOH yields •OOQ_2OOH. The potential energy surface for this radical is given in Figure 4. The bond strength of the formed peroxy bond is 153 kJ mol^{-1}, a value that is slightly higher than the bond strength found for the first molecular oxygen addition step to the primary radical COCOC•. •OOQ_2OOH has three options for subsequent reactions. In the first pathway a hydrogen atom is transferred from the secondary carbon atom to the peroxy group and yields HOOCOC•OCOOH ($HOOU_2$•OOH). The barrier height for this reaction is 66 kJ mol^{-1}, which is lower than those for the two alternative pathways The formed radical can further react to hydroperoxy methyl formate, formaldehyde and a hydroxyl radical via a β-scission reaction or to hydroperoxymethoxy-1,3-dioxetane and a hydroxyl radical.

Both remaining •OOQ_2OOH channels are intramolecular hydrogen abstraction reactions that produce via two different transition states the same unstable HOOCOCOC•OOH intermediate which immediately dissociates to the keto-hydroperoxide (KP_2) and a hydroxyl radical. The difference between both channels is that one is a 1,4 hydrogen atom shift with very high barrier while the second is a 1,8 hydrogen atom shift with a rather low barrier (81 kJ mol^{-1}).

The calculated thermodynamic properties and Arrhenius parameters of all species and reactions depicted in Figures 1–4 are provided in the Supporting information.

5.2. Experimental results and model simulations

The experimental data for the pyrolysis of DMM is depicted in Figure 5. The product species with the highest mole fractions are compared for pyrolysis, fuel-rich, stoichiometric and fuel-lean conditions. At pyrolysis conditions, the DMM conversion starts around 800 K. The main product species that are observed are H_2, CO, CO_2, formaldehyde, methyl formate, methanol and hydrocarbons like methane, ethane and ethylene. The mole fractions of these products are given in Figure 5. The mole fractions of all product species, except for H_2, CO and C_2H_4, have a decreasing trend at higher temperatures. The peak for the formaldehyde, methyl formate and methanol mole fraction is located at

950 K, while for methane and CO_2, this is 1000 K. Some minor product species that are observed are dimethyl ether, propane, propene, 1-butene, 1,3-butadiene and benzene.

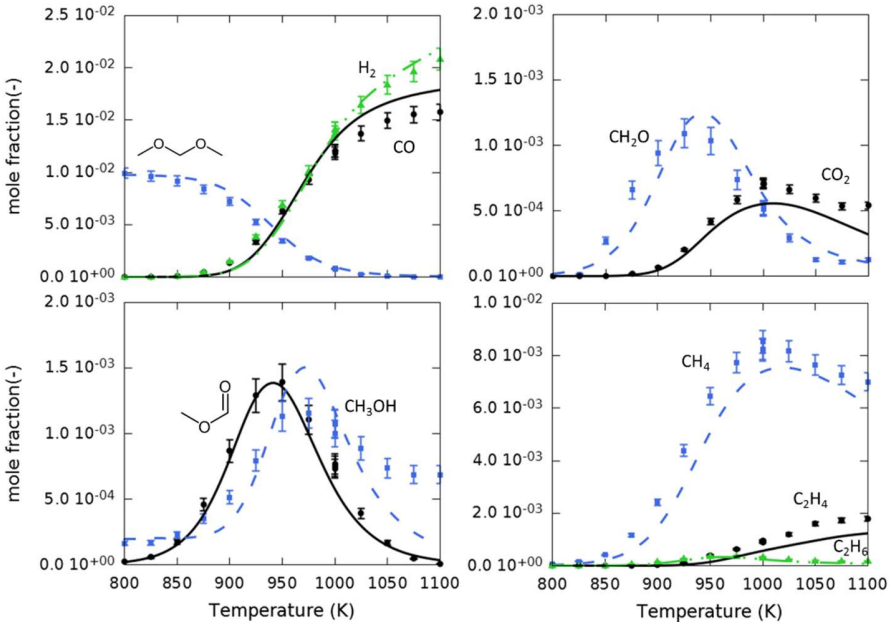

Figure 5: Species mole fractions as a function of temperature for the pyrolysis of DMM. Experiments (symbols) and simulation results (lines) are compared. Experimental conditions are 1.07 bar, 2.83 s residence time and inlet mole fraction of DMM 0.01. Simulations are performed with CHEMKIN software using the continuous stirred-tank reactor option and the new kinetic model.

DMM oxidation experiments have been performed at fuel-rich (φ = 2.0), stoichiometric (φ = 1.0) and fuel-lean (φ = 0.25) conditions and selected profiles are reported in Figures 6, 7 and 8 respectively. Note that the temperature scales are shifted compared to Figure 9. The conversion of DMM starts at lower temperatures if the molecular oxygen content increases. For φ = 2.0, φ = 1.0 and φ = 0.25, the conversion starts around 650 K, 650 K and 550 K respectively. Some low-temperature reactivity is observed for φ = 2.0, φ = 1.0 and φ = 0.25. Because of the small amount, this is not clear from the mole fraction profile of DMM, but it can be noticed in the mole fraction profiles of methyl formate and formaldehyde, which are the main products at low temperatures. The mole fraction profiles of these species show two peaks during oxidation, one peak caused by the low-temperature reactivity and one by the chemistry at higher temperature. Other products formed at low temperatures are CO, methanol and methoxy-1,3-dioxetane. At intermediate temperatures, CO, CO_2, formaldehyde, methyl formate, methanol and hydrocarbons like methane, ethane and ethylene are the main products. The second increase in the mole fraction of formaldehyde, methyl formate, methanol and CO is at 800 K for φ = 2.0 and φ = 1.0 and at 700 K for φ = 0.25. At fuel-lean and stoichiometric conditions, the CO mole fractions go through maxima, indicating that CO is further oxidized to CO_2. In contrast, at fuel-rich conditions, the CO mole fraction profile steadily increases with temperature and CO_2 production is much lower. As expected, the hydrocarbon mole fractions increase with decreasing molecular oxygen mole fraction. The maximum methane mole fractions are at 3.4×10^{-3} at 975 K, 2.7×10^{-3} at 900 K and 1.3×10^{-3} at 875 K for φ = 2.0, φ = 1.0 and φ = 0.25, respectively. For pyrolysis conditions, the peak mole fraction of methane is much higher, i.e. 8.3×10^{-3} at 1000 K.

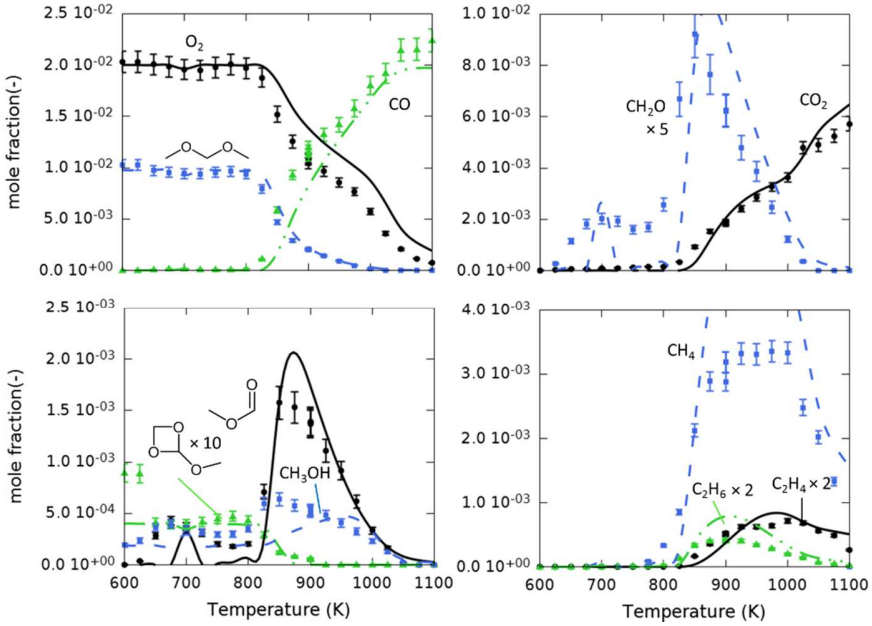

Figure 6: Species mole fractions as a function of temperature for the oxidation of DMM. Experiments (symbols) and simulation results (lines) are compared. Experimental conditions are 1.07 bar, 2.83 s residence time, equivalence ratio of 2.0 and inlet mole fraction of DMM 0.01. Simulations are performed with CHEMKIN software using the continuous stirred-tank reactor option and the new kinetic model. Mole fractions of ethane and ethylene for experimental points and simulations are multiplied by a factor 2, for formaldehyde by a factor 5 and for methoxy-1,3-dioxetane by a factor 10.

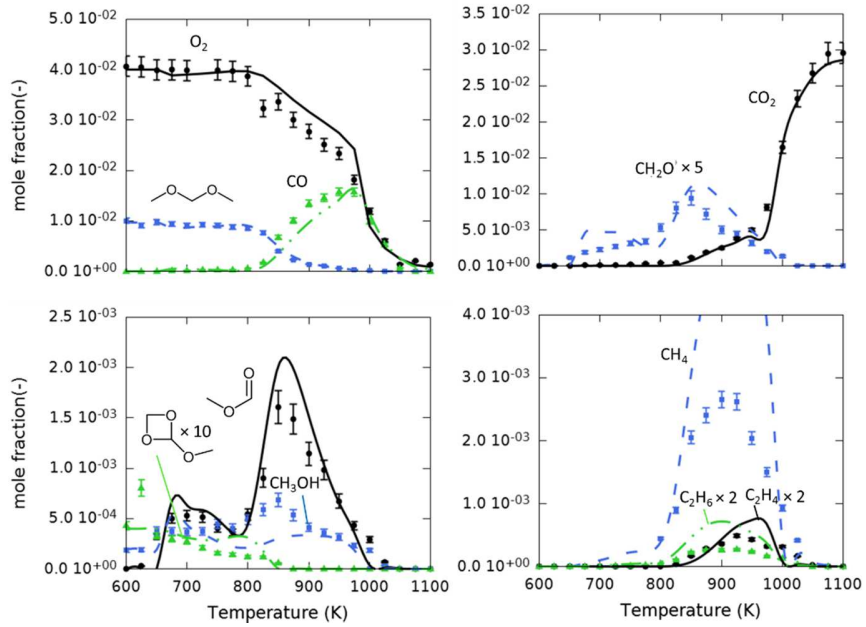

Figure 7: Species mole fractions as a function of temperature for the oxidation of DMM. Experiments (symbols) and simulation results (lines) are compared. Experimental conditions are 1.07 bar, 2.83 s residence time, equivalence ratio of 1.0 and inlet mole fraction of DMM 0.01. Simulations are performed with CHEMKIN software using the continuous stirred-tank reactor option and the new kinetic model. Mole fractions of ethane and ethylene for experimental points and simulations are multiplied by a factor 2, for formaldehyde by a factor 5 and for methoxy-1,3-dioxetane by a factor 10.

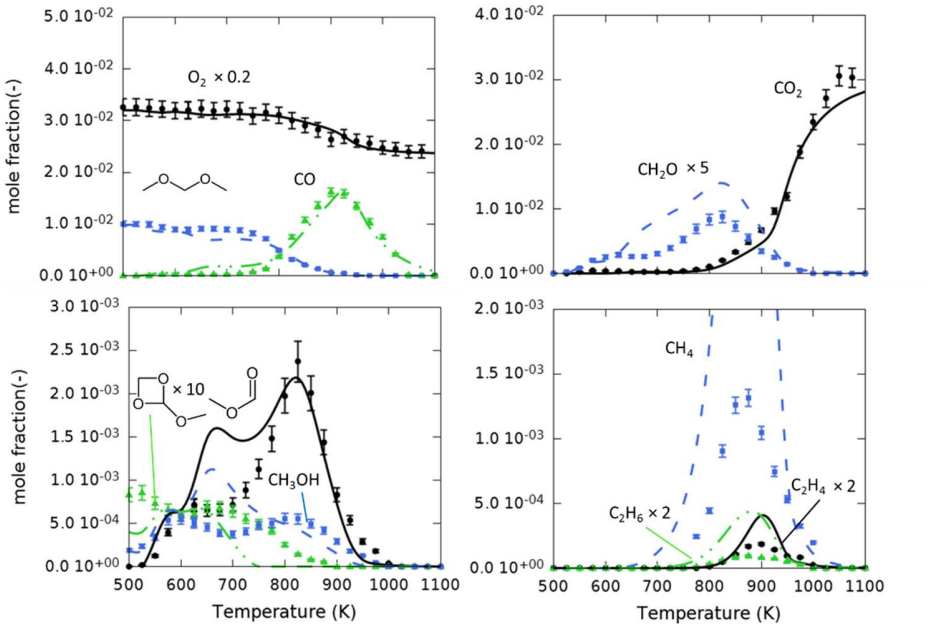

Figure 8: Species mole fractions as a function of temperature for the oxidation of DMM. Experiments (symbols) and simulation results (lines) are compared. Experimental conditions are 1.07 bar, 2.83 s residence time, equivalence ratio of 0.25 and inlet mole fraction of DMM 0.01. Simulations are performed with CHEMKIN software using the continuous stirred-tank reactor option and the new kinetic model. Mole fractions of ethane and ethylene for experimental points and simulations are multiplied by a factor 2, for formaldehyde by a factor 5 and for methoxy-1,3-dioxetane by a factor 10. Mole fractions of molecular oxygen for experimental points and simulations are divided by a factor 5.

The developed kinetic model for the pyrolysis and oxidation of DMM has been used to perform reactor simulations using the continuously stirred tank reactor (CSTR) in CHEMKIN [53]. Simulations results are compared to the experimental data in Figures 5–8. Overall the kinetic model predicts the experimental trends well. For some products, the absolute mole fractions are also well predicted, while the agreement can be improved for others. The largest discrepancies are found for the prediction of alkanes like methane, ethane and ethylene during oxidation. While the trends are captured by the model the peak heights are clearly over predicted. Also the prediction of the low-temperature reactivity can be improved as can be seen in the mole fractions of formaldehyde and methyl formate at the lowest temperatures.

To explain the over prediction of the methane mole fraction, alternative pathways for DMM consumption were searched for. The transition state for the direct decomposition of DMM to formaldehyde and dimethyl ether via a pericyclic reaction was calculated. The barrier for this reaction is equal to 322 kJ mol^{-1}, which indicates that this reaction is negligible at the temperatures considered. Another possible channel is a roaming reaction, similar to the one found for the decomposition of dimethyl ether by Sivaramakrishnan et al. [58]. During the decomposition of DME, this channel only has a small contribution at temperatures higher than 1400 K. For this reason, it is assumed that this reaction will not be important for dimethoxymethane decomposition at the temperature range in this work. Also, the influence of the thermodynamic properties of the main peroxy radicals on the methane mole fraction was tested. Methyl radicals are mainly formed after β-scission reactions that are competing with the addition of

molecular oxygen to the fuel radicals. The conclusion from the test is that changing the enthalpy of e.g. COCOCOO• by 4 kJ mol^{-1} has no influence on the model performance.

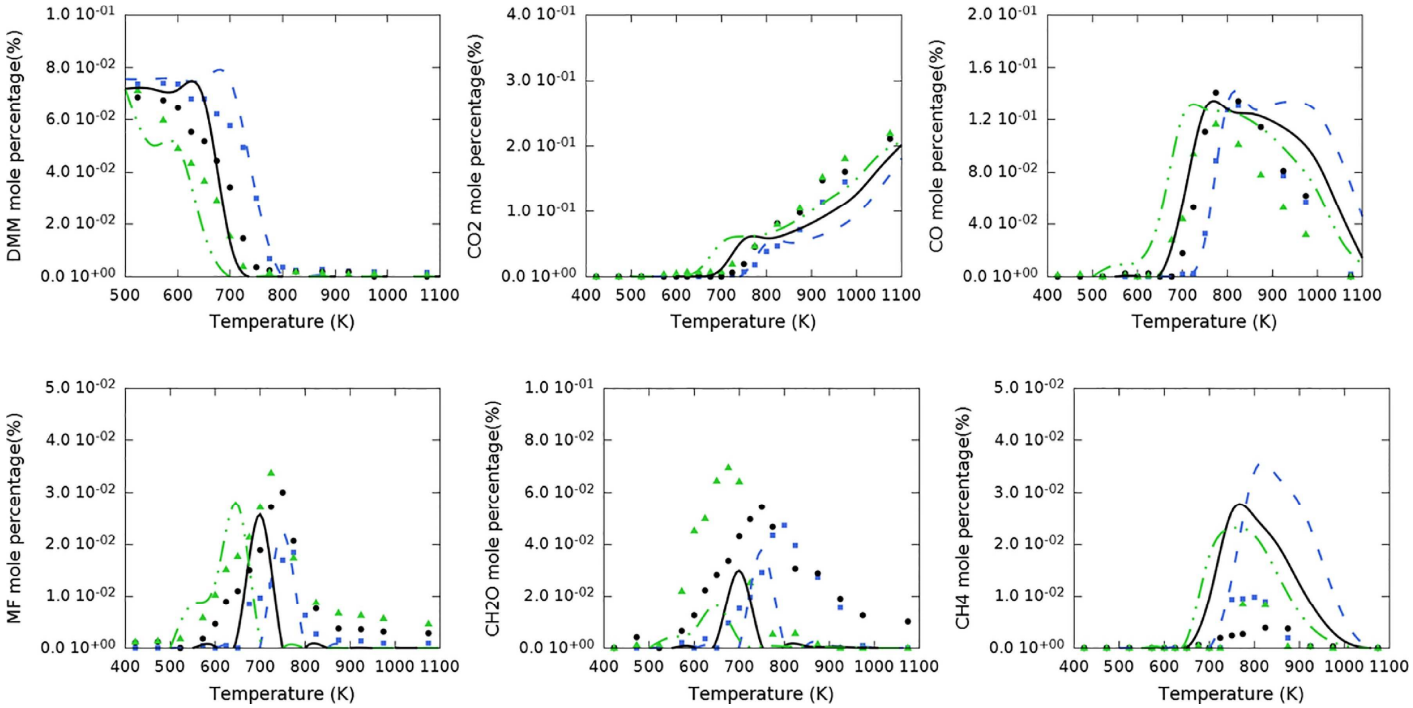

Figure 9: Species mole fractions as a function of temperature for the oxidation of DMM. Experiments (dots), reported by Marrodàn et al. [21], and simulation results (lines) are compared for a pressure equal to 20 bar (blue), 40 bar (black) and 60 bar (green). The air excess ratio is λ = 1.0. Simulations are done with the plug flow reactor option of CHEMKIN [53] software and the new kinetic model. (For interpretation of the references to color in this figure legend, the reader is referred to the web version of this article).

Sensitivity analyses are performed at 700 K and 900 K for φ = 1.0. The results are given in the Supporting information. At these temperatures, the mole fractions of formaldehyde, methyl formate and methane are over predicted by the model. These analyses indicate that consumption and production pathways for methyl radicals, mainly described in the base chemistry, have a large influence on the predictions of the hydrocarbon mole fractions and of the low-temperature reactivity. At 700 K, hydrogen abstraction reactions by methyl peroxy radicals and the reaction between methyl radicals and hydroperoxy radicals play an important role with respect to the DMM, formaldehyde and methyl formate mole fractions, and hence the low-temperature reactivity. The hydrocarbon and methyl radical mole fractions, at 900 K, show large negative sensitivity coefficients for the reaction between methyl radicals and hydroperoxy radicals. The potential energy surface for the reaction between methyl and hydroperoxy radicals was calculated by Jasper et al. [59]. These rate coefficients are used in the base mechanism. Some direct and indirect experimental studies were performed to determine the rate coefficients for these reactions [60-66]; the main observation from these experimental studies were the relatively large error bars for the determined rate coefficients at different temperatures. Because of the large sensitivity coefficient, small changes in the rate coefficients can have a large influence on the hydrocarbon mole fractions. For the hydrogen abstraction reaction by hydroperoxy radicals from formaldehyde, a positive sensitivity coefficient is observed with respect to all hydrocarbon and methyl radical mole fractions.

The kinetic model is also validated against the experimental data published by Marrodàn et al. [21]. This experimental data is acquired in a plug flow reactor, for air excess ratios ranging from 0.7 to 20 and for a large pressure range from 20 to 60 bar. The different type of reactor and the different pressure range make this experimental dataset ideal for validation of the new kinetic model at different conditions. The comparison of simulations with the experimental data for an air excess ratio equal to 1.0 or an equivalence ratio equal to 1.0 is given in Figure 9. For the other air excess ratios, the comparison is given in the Supporting information.

Most species profiles are reasonably well reproduced with respect to trends, peak locations and concentrations. The worst agreement is for formaldehyde, which is often difficult to measure and under predicted by the new DMM model. Similar to the predictions for jet-stirred reactor experiments of the current study, the methane mole fractions of the plug flow study are also clearly over predicted. As discussed above the hydrocarbon mole fractions are very sensitive to the reaction of methyl radicals with hydroperoxy radicals. The methoxy radical formed in this reaction produce formaldehyde at lean conditions. A re-evaluation of this reaction at higher pressures may improve model predictions for both hydrocarbon and formaldehyde mole fractions.

5.3. Reaction pathways leading to low-temperature oxidation

A rate of production analysis is done on the low-temperature oxidation of DMM to identify the pathways that lead to chain branching. In Figure 10 the main pathways are indicated and the relative rate of production is reported at 650 K and 700 K for stoichiometric conditions. Experimentally observed species are highlighted.

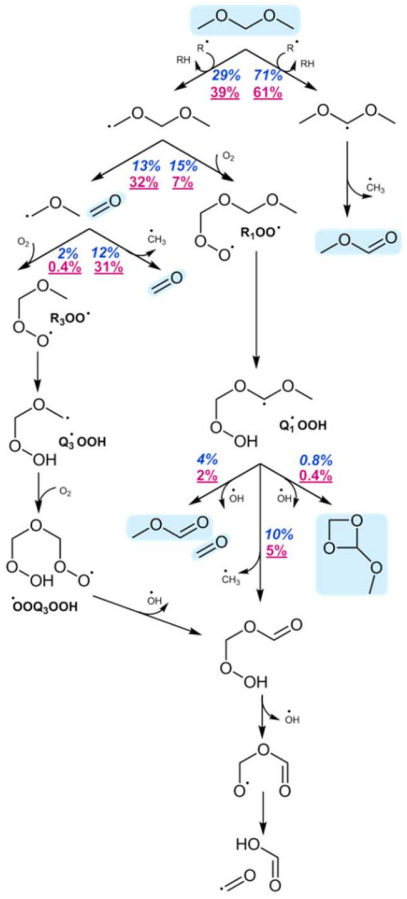

Figure 10: Rate of production analysis to identify important pathways during low-temperature oxidation. Rate of productions relative to the consumption of dimethoxymethane are presented at stoichiometric conditions at 650 K (blue, italic) and 700 K (red, underlined). (For interpretation of the references to color in this figure legend, the reader is referred to the electronic version of this article).

The consumption of DMM, at low temperatures, proceeds completely by hydrogen abstraction reactions. At 650 K, the main abstracting species include molecular oxygen and methyl, hydroperoxy and hydroxyl radicals. At 700 K, the importance of the abstracting species shifts towards hydrogen atoms and hydroxyl and methoxy radicals. The formation of the dimethoxymethyl radical is favored over the production of the methoxymethoxymethyl radical. The dimethoxymethyl radical is completely consumed by a β-scission reaction to form methyl formate and a methyl radical, as can be seen in Figure 10. This is caused by the low barrier which makes this reaction so fast that the addition of molecular oxygen cannot compete. Hence, the major initially formed radical, the dimethoxymethyl radical, does not promote chain branching because of its short lifetime. This is different from the low temperature oxidation of alkanes, where the addition of molecular oxidation is in clear competition with the β-scission reactions at similar temperatures. For comparison, the activation energy for the β-scission of 1-propyl radical is 17 kJ mol^{-1} higher compared to the one for the β-scission of methoxymethyl radical. The higher activation energy results in lower rate coefficients and hence a longer lifetime of these radicals. Methyl formate is not further consumed at these low temperatures.

According to the rate analysis, the consumption of the methoxymethoxymethyl radical via β-scission, forming formaldehyde and a methoxymethyl radical, competes with the addition of molecular oxygen at the experimental conditions. At 650 K, both channels contribute almost equally to the radical consumption while at 700 K the β-scission pathway is favored.

Also the subsequent addition of molecular oxygen to the formed methoxymethyl radical to form $R_3OO\bullet$ is in competition with its β-scission to formaldehyde and a methyl radical. The importance of the β-scission reactions increases with increasing temperature. But even at 650 K only 17% of DMM is converted to peroxy radicals. This explains the lack of pronounced low-temperature oxidation chemistry. Furthermore, some of the subsequent reactions of $R_1OO\bullet$ are chain-propagating and not chain-branching.

$R_1OO\bullet$ can isomerize through three-, six- and eight-membered cyclic transition states. At the conditions selected in this work, the formation of $Q_1\bullet OOH$ via a six-membered ring is preferred, as discussed in paragraph 5.1. The formed hydroperoxide reacts via two β-scission reactions or via cyclic ether formation. Through the main β-scission reaction at both temperatures, hydroperoxy methyl formate and a methyl radical are formed. Subsequent scission of the hydroperoxy group in hydroperoxy methyl formate results in chain branching, as starting from $Q_1\bullet OOH$ three radicals are formed. It should be noted that chain branching occurs through this pathway without the secondary addition of molecular oxygen, as is usually observed for the oxidation of alkanes. Via the minor β-scission reaction, methyl formate, formaldehyde and a hydroxyl radical are produced. The cyclic ether formation, with the production of methoxy-1,3-dioxetane, is the least favored pathway but cannot be neglected.

$R_3OO\bullet$ isomerizes through a six-membered cyclic transition state with the formation of $Q_3\bullet OOH$. The subsequent addition of molecular oxygen to form $\bullet OOQ_3OOH$ is preferred over a β-scission reaction to two formaldehyde molecules and a hydroxyl radical. In a concerted hydrogen atom shift and β-scission reaction of $\bullet OOQ_3OOH$, hydroperoxy methyl formate and a hydroxyl radical are formed. Subsequent reactions convert hydroperoxy methyl formate to formic acid, a formyl radical and a hydroxyl radical. Starting from one methoxymethyl radical and molecular oxygen, two hydroxyl radicals and one formyl radical are formed, hence this is a chain-branching pathway, which however contributes only 2% at 650 K (and less at 700 K) to the total DMM consumption.

Large amounts of methyl radicals are formed during the low-temperature oxidation of dimethoxymethane. The two main pathways are via β-scission reactions starting from dimethoxymethyl and methoxymethyl radicals. Also the formation of methyl radicals from β-scission reactions of Q_1•OOH radicals cannot be neglected at low temperatures. Methyl radicals react mainly via the addition of molecular oxygen. If the temperature increases, the reaction of a methyl radical with a methyl peroxy radical to form two methoxy radicals and the reaction of a methyl radical with a hydroperoxy radical to form a hydroxyl radical and a methoxy radical become important as well. The mole fraction profiles of dimethoxymethane, formaldehyde, methyl formate and other species formed during low-temperature oxidation are very sensitive to some of these reactions and the subsequent reactions of methoxy and methyl peroxy radicals. A sensitivity analysis with respect to the mole fractions of DMM, formaldehyde and methyl formate at 700 K is included in the Supporting information. The low-temperature reactivity depends strongly on the reaction network of the base mechanism for methyl radical reactions. In particular the hydrogen abstraction reactions by methyl peroxy radicals and the reaction between methyl radicals and hydroperoxy radicals are sensitive for the low-temperature reactivity. Therefore, performance improvements of the current DMM model at low temperatures appear to depend on improvements of the low-temperature chemistry of the base mechanism. Putting this in a different way, the new experimental data obtained in this study provide not just the opportunity to improve our understanding of DMM chemistry but provide the chance to validate and improve oxidation base mechanisms as well.

Previous studies on the low-temperature oxidation of dimethyl ether (DME) [8] demonstrate high low-temperature oxidation reactivity and because of its structural similarity with DMM a similar behavior was expected in this study. However, the mole fraction profiles of DMM in Figures 6–8 show that the low-temperature reactivity of DMM is very limited. The difference in low-temperature reactivity between DMM and DME is further analyzed using the new model and a detailed discussion is provided in the Supporting information. Briefly, in DME oxidation about 23% of DME is converted through a pathway that leads to chain branching. For DMM oxidation, two chain-branching producing pathways are active, however they contribute to only 12% of the converted DMM. Furthermore, chain-branching of DME results in two reactive hydroxyl radicals, while only one hydroxyl radical and one, at low temperature less reactive, methyl radical is formed in the major chain-branching pathway in DMM oxidation.

5.4. Oxidation at intermediate temperatures

At temperatures above 750 K, the addition of molecular oxygen to the primary radical formed from dimethoxymethane and to a methoxymethyl radical becomes negligible. Above these temperatures and at pyrolysis conditions, only a few reaction pathways are important for the decomposition of dimethoxymethane. These pathways at fuel-rich and pyrolysis conditions at 900 K are presented in Figure 11. Species that are detected experimentally are highlighted.

Dimethoxymethane is again mainly consumed by hydrogen abstraction reactions but the C-O bond scission reaction forming methoxy and methoxymethyl radicals also contributes slightly, in particular at higher temperatures and pyrolysis conditions. The main abstracting species during fuel-rich oxidation at 900 K are hydroxyl radicals and hydrogen atoms. Also methyl and hydroperoxy radicals are important at 900 K, but their role diminishes as temperature increases. In case of pyrolysis, hydrogen atoms and methyl radicals are the main abstracting species and hydrogen abstractions by methoxy radicals make minor contributions. At 900 K, methyl radicals are the most important, but as temperature increases the role of hydrogen atoms grows.

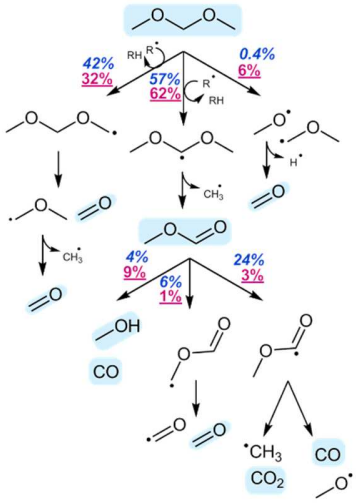

Figure 11: Rate of production analysis for the oxidation at intermediate temperatures and pyrolysis. Rate of productions relative to the consumption of dimethoxymethane are presented at 900 K for fuel-rich (blue, italic) and pyrolysis (red, underlined) conditions. (For interpretation of the references to color in this figure legend, the reader is referred to the web version of this article).

The radicals formed from dimethoxymethane react via β-scission reactions. Through these reactions, formaldehyde and methyl formate are formed. Methyl formate is further consumed either by direct CO elimination forming methanol as byproduct or by hydrogen abstraction reactions. Hydrogen abstraction reactions dominate at fuel-rich conditions and result mainly in the production of the methoxy formyl radical. This radical decomposes primarily by a β-scission reaction to CO_2 and a methyl radical or as a minor channel via α-scission to CO and a methoxy radical. Hydrogen abstraction from the methyl group in methyl format and subsequent β-scission yields formaldehyde and the formyl radical. At the pyrolysis conditions used in this work, the consumption rate of methyl formate is still low at 900 K, but it increases rapidly with temperature. It is mainly consumed unimolecular by CO elimination forming methanol. At 1000 K, more than 77% of methyl formate is consumed through this channel.

The simulated mole fraction profile of methyl formate at lean conditions shows three maxima, as can be seen in Figure 8. These peaks are the result of the complexity of the methyl formate chemistry at these conditions and the different temperature dependencies of competing reactions. At the lowest temperatures the β-scission of dimethoxymethyl radical and the β-scission of Q_1•OOH compete. At higher temperatures various hydrogen abstraction reactions become important. The consumption of methyl formate by the hydrogen abstraction reaction by a hydroxyl radical from the carbonyl group gains importance at 700 K (φ = 0.25) and causes the methyl formate mole fraction to decrease at this temperature. At even higher temperatures other hydrogen abstraction reactions become important and cause another maximum at 900 K (φ = 0.25).

Note that methyl radicals are produced by the three pathways shown in Figure 11. From Figure 5, it becomes clear that the current model captures this chemistry very well as the methane, ethane and ethylene yields as a function of temperature are nicely reproduced. This suggests that the overprediction of these hydrocarbons is caused by the oxidation chemistry, in agreement with the conclusions drawn earlier based on the rate of production analysis for the stoichiometric mixture.

6. Conclusions

New experimental data is acquired in an isothermal quartz jet-stirred reactor setup. This dataset captures the low- and intermediate-temperature oxidation and pyrolysis of DMM and is used for validation of a newly generated kinetic model. The low-temperature chemistry of dimethoxymethane has been studied in detail by investigating the relevant potential energy surfaces at the CBS-QB3 level of theory and first-principles based thermochemical data are calculated. The software Genesys is used to generate an elementary step kinetic model for DMM pyrolysis and oxidation using quantum mechanically calculated thermodynamic properties and kinetics as input. For the thermodynamic properties of the smallest species and the kinetics of the reactions between those species, the base mechanism developed by Metcalfe et al. (AramcoMech 1.3) has been used. The more recently published version of this base mechanism fails to predict CO_2, methyl formate and methanol mole fractions during the pyrolysis of dimethoxymethane. The discrepancies have been assigned to one missing reaction ($CH_3OCHO(+ M) = CO + HOCH_3(+ M)$) and different Arrhenius parameters for two other reactions ($CH_3OCO = CO + OCH_3$ and $CH_3OCO = CO_2 + CH_3$). The final kinetic model predicts the overall trends observed during experiments well, in particular the pyrolysis data. Discrepancies exist for some hydrocarbon mole fractions at oxidative conditions and for the low-temperature oxidation regime. These discrepancies are very sensitive to reactions involving methyl radicals because of the high methyl radical mole fraction observed during the oxidation of dimethoxymethane.

The kinetic model has also been validated with experimental data published by Marrodàn et al. This experimental data is acquired in a plug flow reactor at elevated pressures. Overall the model performs well for the different conditions and different reactor type. The main discrepancies are similar to the ones observed previous, i.e. the over production of the hydrocarbon mole fractions. Also the experimental dataset in a jet-stirred reactor reported by Daly et al. and the dataset for lean and rich flames acquired by Dias et al. are used to successfully validate the kinetic model. The overall good performance of the kinetic model for all experimental datasets demonstrates the strength of developing a kinetic model based on first principles.

One point of interest was the extent at which low-temperature oxidation occurs with DMM as fuel. A rate of production analysis at low temperatures allowed to identify two chain branching pathways, needed for low-temperature oxidation. Both chain branching pathways start from the methoxymethoxymethyl radical, while the in higher amounts produced dimethoxymethyl radical decomposes so fast to a methyl radical and methyl formate that the addition of molecular oxygen cannot compete. The methoxymethoxymethyl radical either decomposes to formaldehyde and a methoxymethyl radical or adds to molecular oxygen. The methoxymethyl radical formed in the first pathway reacts the same way as in DME oxidation and chain branching channel results from typical second oxygen addition chemistry. The second chain branching pathway, starting with molecular oxygen addition to methoxymethoxymethyl radicals is unique because it does not require the addition of a second molecular oxygen. Since DMM is mostly consumed forming a radical that does not support chain branching, the limited low-temperature chemistry of DMM is easily explained.

Acknowledgments

This work was carried out using the STEVIN Supercomputer Infrastructure at Ghent University, funded by Ghent University, the Flemish Supercomputer Center (VSC), the Hercules Foundation and the Flemish Government –

department EWI. The authors would like to acknowledge the financial support from the SBO proposals “Bioleum” and “Arboref” supported by the Institute for promotion of Innovation through Science and Technology in Flanders (IWT), the COST Action CM1404 “Chemistry of smart energy carriers and technologies” and the European Research Council under the European Union's Seventh Framework Programme (FP7/2007-2013)/ERC Grant agreement no. 290793.

Supplementary materials

- Supporting Information
- Detailed kinetic model with thermodynamic properties under Chemkin format
- Excel spreadsheet with experimental data

References

1. J. Abboud; J. Schobing; G. Legros; J. Bonnety; V. Tschamber; A. Brillard; G. Leyssens; V. Lauga; E. E. Iojoiu; P. Da Costa, Fuel 193 (2017) 241-253
2. L. Coniglio; H. Bennadji; P. A. Glaude; O. Herbinet; F. Billaud, Progress in Energy and Combustion Science 39 (4) (2013) 340-382
3. E. Khalife; M. Tabatabaei; A. Demirbas; M. Aghbashlo, Progress in Energy and Combustion Science 59 (2017) 32-78
4. K. Kohse-Höinghaus; P. Oßwald; T. A. Cool; T. Kasper; N. Hansen; F. Qi; C. K. Westbrook; P. R. Westmoreland, Angewandte Chemie International Edition 49 (21) (2010) 3572-3597
5. A. K. Agarwal, Progress in Energy and Combustion Science 33 (3) (2007) 233-271
6. N. M. Ribeiro; A. C. Pinto; C. M. Quintella; G. O. da Rocha; L. S. G. Teixeira; L. L. N. Guarieiro; M. do Carmo Rangel; M. C. C. Veloso; M. J. C. Rezende; R. Serpa da Cruz; A. M. de Oliveira; E. A. Torres; J. B. de Andrade, Energy & Fuels 21 (4) (2007) 2433-2445
7. W. Ying; L. Genbao; Z. Wei; Z. Longbao, Fuel Processing Technology 89 (12) (2008) 1272-1280
8. A. Rodriguez; O. Frottier; O. Herbinet; R. Fournet; R. Bounaceur; C. Fittschen; F. Battin-Leclerc, J. Phys. Chem. A 119 (28) (2015) 7905-7923
9. M. Härtl; P. Seidenspinner; E. Jacob; G. Wachtmeister, Fuel 153 (2015) 328-335
10. Z. Wang; H. Liu; J. Zhang; J. Wang; S. Shuai, Energy Procedia 75 (2015) 2337-2344
11. X. Zhang; A. Kumar; U. Arnold; J. Sauer, Energy Procedia 61 (2014) 1921-1924
12. J. Burger; M. Siegert; E. Ströfer; H. Hasse, Fuel 89 (11) (2010) 3315-3319
13. B. Lumpp; D. Rothe; C. Pastötter; R. Lämmermann; E. Jacob, MTZ worldwide eMagazine 72 (3) (2011) 34-38
14. E. Jacob Fuel for compression-ignition engines based on monooxymethylene dimethylether. US 9447355 B2, 2014.
15. H. Schelling; E. Stroefer; R. Pinkos; A. Haunert; G. D. Tebben; H. Hasse; S. Blagov Method for Producing Polyoxymethylene Dimethyl Ethers. US 9266990 B2, 2007.
16. C. A. Daly; J. M. Simmie; P. Dagaut; M. Cathonnet, Combustion and Flame 125 (3) (2001) 1106-1117
17. V. Dias; X. Lories; J. Vandooren, Combust. Sci. Technol. 182 (4-6) (2010) 350-364
18. V. Dias; C. Renard; J. Vandooren, Z. Phys. Chemie-Int. J. Res. Phys. Chem. Chem. Phys. 223 (4-5) (2009) 565-577
19. V. Dias; J. Vandooren, Combustion and Flame 158 (5) (2011) 848-859
20. L. Marrodan; F. Monge; A. Millera; R. Bilbao; M. U. Alzueta, Combust. Sci. Technol. 188 (4-5) (2016) 719-729
21. L. Marrodan; E. Royo; A. Millera; R. Bilbao; M. U. Alzueta, Energy & Fuels 29 (5) (2015) 3507-3517

22. R. Van de Vijver; N. M. Vandewiele; A. G. Vandeputte; K. M. Van Geem; M. F. Reyniers; W. H. Green; G. B. Marin, Chem. Eng. J. 278 (2015) 385-393
23. N. M. Vandewiele; K. M. Van Geem; M. F. Reyniers; G. B. Marin, Chem. Eng. J. 207 (2012) 526-538
24. O. Herbinet; F. Battin-Leclerc, Int. J. Chem. Kinet. 46 (10) (2014) 619-639
25. J. A. Montgomery; M. J. Frisch; J. W. Ochterski; G. A. Petersson, J. Chem. Phys. 110 (6) (1999) 2822-2827
26. M. J. Frisch, G. W. Trucks, H. B. Schlegel, G. E. Scuseria, M. A. Robb, J. R. Cheeseman, G. Scalmani, V. Barone, B. Mennucci, G. A. Petersson, H. Nakatsuji, M. Caricato, X. Li, H. P. Hratchian, A. F. Izmaylov, J. Bloino, G. Zheng, J. L. Sonnenberg, M. Hada, M. Ehara, K. Toyota, R. Fukuda, J. Hasegawa, M. Ishida, T. Nakajima, Y. Honda, O. Kitao, H. Nakai, T. Vreven, J. A. Montgomery, Jr., J. E. Peralta, F. Ogliaro, M. Bearpark, J. J. Heyd, E. Brothers, K. N. Kudin, V. N. Staroverov, R. Kobayashi, J. Normand, K. Raghavachari, A. Rendell, J. C. Burant, S. S. Iyengar, J. Tomasi, M. Cossi, N. Rega, J. M. Millam, M. Klene, J. E. Knox, J. B. Cross, V. Bakken, C. Adamo, J. Jaramillo, R. Gomperts, R. E. Stratmann, O. Yazyev, A. J. Austin, R. Cammi, C. Pomelli, J. W. Ochterski, R. L. Martin, K. Morokuma, V. G. Zakrzewski, G. A. Voth, P. Salvador, J. J. Dannenberg, S. Dapprich, A. D. Daniels, Ö. Farkas, J. B. Foresman, J. V. Ortiz, J. Cioslowski, and D. J. Fox, in: Gaussian, Inc.: Wallingford CT, 2009.
27. R. Van de Vijver; K. p. M. G. B. p. Van Geem. Automatische ab-initioberekeningen voor het genereren van kinetische modellen van gasfaseprocessen. PhD Thesis, Gent Universiteit, 2017.
28. A. L. L. East; L. Radom, J. Chem. Phys. 106 (16) (1997) 6655-6674
29. L. A. Curtiss; K. Raghavachari; P. C. Redfern; J. A. Pople, J. Chem. Phys. 106 (3) (1997) 1063-1079
30. G. A. Petersson; D. K. Malick; W. G. Wilson; J. W. Ochterski; J. A. Montgomery; M. J. Frisch, J. Chem. Phys. 109 (24) (1998) 10570-10579
31. C. Eckart, Physical Review 35 (11) (1930) 1303-1309
32. J. Prager; H. N. Najm; J. Zádor, Proc. Combust. Inst. 34 (1) (2013) 583-590
33. P. D. Paraskevas; M. K. Sabbe; M. F. Reyniers; N. Papayannakos; G. B. Marin, Chem.-Eur. J. 19 (48) (2013) 16431-16452
34. S. M. Villano, L. K. Huynh, H. H. Carstensen, A. M. Dean, J. Phys. Chem. A, 115 (46) (2011) 13425–13442
35. H. H. Carstensen; A. M. Dean, J. Phys. Chem. A 113 (2) (2009) 367-380
36. H. H. Carstensen; A. M. Dean, Int. J. Chem. Kinet. 44 (1) (2012) 75-89
37. A. G. Vandeputte; M. K. Sabbe; M. F. Reyniers; V. Van Speybroeck; M. Waroquier; G. B. Marin, J. Phys. Chem. A 111 (46) (2007) 11771-11786
38. S. W. Benson; J. H. Buss, J. Chem. Phys. 29 (3) (1958) 546-572
39. T. H. Lay; J. W. Bozzelli; A. M. Dean; E. R. Ritter, J. Phys. Chem. 99 (39) (1995) 14514-14527
40. M. K. Sabbe; M. Saeys; M. F. Reyniers; G. B. Marin; V. Van Speybroeck; M. Waroquier, J. Phys. Chem. A 109 (33) (2005) 7466-7480
41. M. K. Sabbe; M. F. Reyniers; V. Van Speybroeck; M. Waroquier; G. B. Marin, Chem. Phys. Chem. 9 (1) (2008) 124-140
42. M. Saeys; M. F. Reyniers; G. B. Marin; V. Van Speybroeck; M. Waroquier, Aiche J. 50 (2) (2004) 426-444
43. M. K. Sabbe; A. G. Vandeputte; M. F. Reyniers; M. Waroquier; G. B. Marin, Phys. Chem. Chem. Phys. 12 (6) (2010) 1278-1298
44. P. D. Paraskevas; M. K. Sabbe; M. F. Reyniers; N. Papayannakos; G. B. Marin, Chem. Phys. Chem. 15 (9) (2014) 1849-1866
45. P. D. Paraskevas; M. K. Sabbe; M. F. Reyniers; N. G. Papayannakos; G. B. Marin, J. Phys. Chem. A 119 (27) (2015) 6961-6980

46. P. D. Paraskevas; M. K. Sabbe; M. F. Reyniers; N. G. Papayannakos; G. B. Marin, J. Phys. Chem. A 118 (40) (2014) 9296-9309
47. M. K. Sabbe; M. F. Reyniers; M. Waroquier; G. B. Marin, ChemPhysChem 11 (1) (2010) 195-210
48. P. D. Paraskevas; M. K. Sabbe; M. F. Reyniers; G. B. Marin; N. G. Papayannakos, Aiche J. 62 (3) (2016) 802-814
49. R. Sivaramakrishnan; J. V. Michael, J. Phys. Chem. A 113 (17) (2009) 5047-5060
50. L. M. Cai; H. Pitsch; S. Y. Mohamed; V. Raman; J. Bugler; H. Curran; S. M. Sarathy, Combust. Flame 173 (2016) 468-482
51. S. M. Sarathy; C. K. Westbrook; M. Mehl; W. J. Pitz; C. Togbe; P. Dagaut; H. Wang; M. A. Oehlschlaeger; U. Niemann; K. Seshadri; P. S. Veloo; C. Ji; F. N. Egolfopoulos; T. Lu, Combust. Flame 158 (12) (2011) 2338-2357
52. J. Bugler; K. P. Somers; E. J. Silke; H. J. Curran, J. Phys. Chem. A 119 (28) (2015) 7510-7527
53. W. K. Metcalfe; S. M. Burke; S. S. Ahmed; H. J. Curran, Int. J. Chem. Kinet. 45 (10) (2013) 638-675
54. R. J. Kee; F. M. Rupley; J. A. Miller; M. E. Coltrin; J. F. Grcar; E. Meeks; H. K. Moffat; A. E. Lutz; G. Dixon-Lewis; M. D. Smooke; J. Warnatz; G. H. Evans; L. R. S.; R. E. Mitchell; L. R. Petzold; W. C. Reynolds; M. Caracotsios; W. E. Stewart; P. Glarborg; C. Wang; O. Adigun, in: 15101 ed.; Reaction Design, Inc.: San Diego (CA), 2010.
55. S. M. Burke; W. Metcalfe; O. Herbinet; F. Battin-Leclerc; F. M. Haas; J. Santner; F. L. Dryer; H. J. Curran, Combust. Flame 161 (11) (2014) 2765-2784
56. L. K. Huynh; K. C. Lin; A. Violi, J. Phys. Chem. A 112 (51) (2008) 13470-13480
57. S. M. Villano; L. K. Huynh; H. H. Carstensen; A. M. Dean, J. Phys. Chem. A 116 (21) (2012) 5068-5089
58. R. Sivaramakrishnan; J. V. Michael; A. F. Wagner; R. Dawes; A. W. Jasper; L. B. Harding; Y. Georgievskii; S. J. Klippenstein, Combust. Flame 158 (4) (2011) 618-632
59. A. W. Jasper; S. J. Klippenstein; L. B. Harding, Proc. Combust. Inst. 32 (1) (2009) 279-286
60. M. B. Colket; D. W. Naegeli; I. Glassman, Symposium (International) on Combustion 16 (1) (1977) 1023-1039
61. N. K. Srinivasan; J. V. Michael; L. B. Harding; S. J. Klippenstein, Combust. Flame 149 (1) (2007) 104-111
62. D. L. Baulch; C. J. Cobos; R. A. Cox; C. Esser; P. Frank; T. Just; J. A. Kerr; M. J. Pilling; J. Troe; R. W. Walker; J. Warnatz, J. Phys. Chem. Ref. Data 21 (3) (1992) 411-734
63. J. J. Scire; S. D. Klotz; F. L. Dryer, Z. Phys. Chemie-Int. J. Res. Phys. Chem. Chem. Phys. 215 (2001) 1011-1023
64. J. J. Scire; R. A. Yetter; F. L. Dryer, Int. J. Chem. Kinet. 33 (2) (2001) 75-100
65. Z. Hong; D. F. Davidson; K.-Y. Lam; R. K. Hanson, Combust. Flame 159 (10) (2012) 3007-3013
66. M. Sangwan; L. N. Krasnoperov, J. Phys. Chem. A 117 (14) (2013) 2916-2923